liquid plus CDW theory and given the relatively low ordering temperature (~30 to 70 K) (*3, 24, 30*), one would expect 1D behavior only at an energy scale much lower than 500 meV. The solution to this dramatic departure from the Fermi liquid paradigm appears to call for a different basic starting point. Instead of quasiparticles, one may start with stripes that are at least locally stable up to very high energy, as reflected in ARPES data that are mainly sensitive to the local information at such high energy. The fluctuation of the stripes may give rise to the global 2D character in the intermediate energy and temperature scale. The ordering seen in neutron-scattering and nuclear quadrupole resonance (NQR) experiments is the freezing out of these fluctuations (*3, 24*) that results in the long range order. In this sense, one may consider that the ARPES data reflect the local amplitude of stripe formation, which is of high energy scale, whereas the neutron-scattering and NQR data reflect the phase of stripe correlation. This discussion then leads to another paradox, which has to do with the edge dispersion perpendicular to stripes. How can charges, which are already confined to stripes at energy scale of 500 meV, experience perpendicular motion with the dispersion of 200 meV (Fig. 5A)? This may be related to the paradox that the spectra are extremely broad in energy yet sharply defined in momentum, as reflected in the $\pi/4$ boundary separating the high and low spectral weight regions. We have no clear answer, but we speculate that it is related to the fact that stripes tend to be 1/4 filled (*3, 14, 15, 22*) and the stripe fluctuations can give charge motions (coherent or incoherent) perpendicular to stripes. Further theoretical work that takes into account the energetics of charge motion in an antiferromagnetic background and stripe potential (*36*) and investigates the connection of the edge dispersion to the transverse stripe fluctuation (*8–13*) is needed to address these issues.

References and Notes

1. S. A. Kivelson and V. J. Emery, in *Strongly Correlated Electronic Materials: The Los Alamos Symposium 1993*, K. S. Bedell *et al.*, Eds. (Addison-Wesley, Reading, MA, 1994), pp. 619–650; V. J. Emery, S. A. Kivelson, O. Zacher, *Phys. Rev. B* **56**, 6120 (1997).
2. J. Zaanen and O. Gunnarson, *Phys. Rev. B* **40**, 7391 (1989).
3. J. M. Tranquada, B. J. Sternlieb, J. D. Axe, Y. Nakamura, S. Uchida, *Nature* **375**, 561 (1995); J. M. Tranquada, N. Ichikawa, S. Uchida, *Phys. Rev. B* **59**, 14712 (1999).
4. D. Poilbanc and T. M. Rice, *Phys. Rev. B* **39**, 9749 (1989).
5. H. J. Schulz, *J. Phys.* **50**, 2833 (1989).
6. C. Castellani, C. D. Castro, M. Grilli, *Phys. Rev. Lett.* **75**, 4650 (1995).
7. A. H. Castro Neto and D. Hone, *ibid.* **76**, 2165 (1996).
8. J. Zaanen, M. L. Horbach, W. V. Saarloos, *Phys. Rev. B* **53**, 8671 (1996).
9. H. Eskes, R. Grimberg, W. Van Saarloos, J. Zaanen, *ibid.* **54**, R724 (1996); H. Eskes, O. Y. Osman, R. Grimberg, W. V. Saarloos, J. Zaanen, *ibid.* **58**, 6963 (1998).
10. C. Morais Smith, Y. A. Mimashko, N. Hasselmann, A. O. Calderia, *ibid.* **58**, 453 (1998).
11. S. A. Kivelson, E. Fradkin, V. J. Emery, *Nature* **393**, 550 (1998).
12. J. Zaanen, O. Y. Osman, W. Van Saarloos, *Phys. Rev. B* **58**, R11868 (1998).
13. N. Hasselmann, A. H. Castro Neto, C. Morais Smith, Y. Dimashko, *Phys. Rev. Lett.* **82**, 2135 (1999).
14. J. Zaanen and A. M. Oles, *Ann. Phys.* **5**, 224 (1996).
15. C. Nayak and F. Wilczek, *Phys. Rev. Lett.* **78**, 2465 (1997).
16. M. I. Salkola, V. J. Emery, S. A. Kivelson, *ibid.* **77**, 155 (1996).
17. S. R. White and D. J. Scalapino, *ibid.* **81**, 3227 (1998).
18. T. Tohyama, S. Nagai, Y. Shibata, S. Maekawa, *ibid.* **82**, 4910 (1999).
19. A. V. Balatsky and P. Bourges, *ibid.*, p. 5337.
20. B. O. Wells *et al.*, *Science* **277**, 1067 (1997).
21. G. Aeppli *et al.*, *ibid.* **278**, 1432 (1997).
22. K. Yamada *et al.*, *Phys. Rev. B* **57**, 6165 (1998); Y. S. Lee *et al.*, preprint available at xxx.lanl.gov/abs/cond-mat/9902157.
23. H. A. Mook *et al.*, *Nature* **395**, 580 (1998).
24. A. W. Hunt, P. M. Singer, K. R. Thurber, T. Tmai, *Phys. Rev. Lett.* **82**, 4300 (1999).
25. The ARPES data were recorded at the beamline 10.0.1.1 of the Advanced Light Source. Fifty-five–electron volt photon energy was used for more efficient *k*-space sampling. With the use of the angular mode of the Scienta analyzer, the momentum resolution was 0.02π. The energy resolution was detuned from its optimal 7 meV to 16 meV so that a few thousand spectra with sufficient statistics could be obtained during the lifetime of a cleaved surface. For example, the 500 spectra presented in Fig. 1 of this paper were recorded within the first 3 hours after the cleaving; the results are robust from cleave to cleave. The vacuum during the measurement was ~2 to 5 × 10^{-11} torr. LEED experiments were performed to check the surface structure, yielding the expected four-fold symmetry. The Nd-LSCO sample was grown with the traveling floating zone method. The same class of samples has been used for neutron-scattering experiments (*3*).
26. The angular mode of the analyzer allows us to cover nearly a whole quadrant along k_x with 48 points at the same time, which correspond to the spectra in Fig. 1, A to J; the whole BZ is then measured by taking various k_y cuts.
27. Here the "occupied" area means that the occupation probability is high. In an interacting system, $n(k)$ will not be zero even in the region where the "band" is above the Fermi level.
28. P. H. Dickinson and S. Doniach, *Phys. Rev. B* **47**, 11447 (1993).
29. Y. Nakamura and S. Uchida, *ibid.* **46**, 5841 (1992).
30. M. V. Zimmermann *et al.*, *Europhys. Lett.* **41**, 629 (1998).
31. A. Ino *et al.*, preprint available at xxx.lanl.gov/abs/cond-mat/9809311; A. Ino *et al.*, preprint available at xxx.lanl.gov/abs/cond-mat/9902048.
32. A. G. Loeser *et al.*, *Science* **273**, 325 (1996); D. S. Marshall *et al.*, *Phys. Rev. Lett.* **76**, 4841 (1996); H. Ding *et al.*, *Nature* **382**, 51 (1996).
33. A. V. Balatsky and Z.-X. Shen, *Science* **284**, 1137 (1999).
34. From the outset, we note that this gapping effect is not caused by the extrinsic loss mechanism suggested recently [R. Joynt, *Science* **284**, 777 (1999)], which cannot explain the angular dependence of the gap. In this case, the smallest gap is 5 meV or less, further suggesting that the extrinsic loss mechanism is not an issue here.
35. Although no data for $|k_y| = 0.25\pi$ are available, because the dispersion with k_y is very minimal, the $|k_y| = 0.15\pi$ result is a good indicator of the gap.
36. E. Dagotto, *Rev. Mod. Phys.* **66**, 763 (1994).

37. We thank E. D. Lu, J. Denlinger, J. Bozek, and D. H. Lu for technical support and S. A. Kivelson, J. Zaanen, R. B. Laughlin, D. van der Marel, A. Fujimori, H. Fukuyama, C. D. Castro, W. Hanke, and J. M. Tranquada for helpful comments. The experiment was performed at the Advanced Light Source of the Lawrence Berkeley National Laboratory, which is operated by the U.S. Department of Energy's Office of Basic Energy Science, Division of Material Science. The division also provided support for the Stanford Synchrotron Radiation Laboratory experimental effort and end-station development through grant DE-FG03-96ER45594. The Stanford University work was also supported by NSF grant DMR-9705210.

21 June 1999; accepted 31 August 1999

Evidence of Nonlinear Elasticity of the Crust from the Mw7.6 Manyi (Tibet) Earthquake

Gilles Peltzer,[1]* Frédéric Crampé,[2] Geoffrey King[2]

Satellite synthetic aperture radar (SAR) interferometry shows that the magnitude 7.6 Manyi earthquake of 8 November 1997 produced a 170-kilometer-long surface break with up to 7 meters of left-lateral slip, reactivating a N76°E quaternary fault in western Tibet. The radar interferometric map reveals asymmetric, along-strike displacement profiles between the two sides of the surface rupture, a pattern that cannot be explained with linear elastic theory. This observation suggests that the elastic moduli of the crust in tension and in compression are different because of the presence of cracks in the crust at shallow depth. A model indicates that a ratio of 2 between compressive and tensile elastic moduli can account for the observed asymmetry, a ratio that is consistent with laboratory and borehole measurements.

Geodetic measurements of the static surface displacement field produced by large earthquakes provide information about their source mechanism. Linear models of dislocation in an elastic half-space (*1*) are widely used to represent earthquake faults and generally provide a satisfactory fit to near- and far-field displacement data obtained with conventional geodetic techniques (*2*). However, laboratory experiments and in situ measurements in boreholes have shown that many crustal rocks exhibit a nonlinear elastic behavior in compression and tension with a dependence of the Young's modulus on the minimum principal stress (*3*). The effects of nonlinear elastic properties of crustal rocks

have never been observed in geodetic signals associated with elastic crustal strain because of the low sampling density of techniques that make use of ground-based instrument arrays (*4*). Here we have used SAR interferometry (*5*) to analyze coseismic surface displacement in the near field of the 1997 Manyi, Tibet, earthquake rupture.

The magnitude (Mw) 7.6 Manyi earthquake occurred on 8 November 1997 in western Tibet with a hypocenter depth of 15 km. The region is flat with an elevation of 5000 m near the western end of the Kunlun fault (*6*). The focal mechanism (*7*) indicates left-lateral, strike-slip motion on a fault plane parallel to a mapped quaternary fault (*8*) (Fig. 1). The aftershocks define an east-northeast trend approximately aligned with the fault (*9*). To map the earthquake displacement, we combined SAR images acquired by the European Remote Sensing satellite (ERS-2) on three adjacent tracks before and after the event (*10*) (Fig. 1). The topographic signal was removed from interferograms (*11*) by use of a digital elevation model (*12*). The resulting interferogram shows the surface displacement produced by the earthquake in the direction parallel to the radar line of sight (Fig. 2A) (*13*).

The three-track mosaic (Fig. 2A) covers the 170-km-long section of the fault that ruptured during the earthquake. The two half-lobe patterns north and south of the rupture are consistent with a left-lateral motion on the fault. The maximum range displacement is observed immediately east of the center of the rupture and exceeds 1.2 m on each side of the fault (Fig. 2B). Assuming left-lateral slip on a N76°E fault, this indicates that the total relative offset reached 7 m. The smoothness of the contours of the surface displacement field suggests a smooth fault geometry and a smooth distribution of slip on the fault at shallow depth. The displacement profiles perpendicular to the fault indicate a relatively shallow fault depth. Assuming a uniform slip distribution with depth, elastic dislocation modeling (*1*) shows that a fault depth of ~8 km is required to fit the observed displacement profiles (Fig. 2B).

Surface condition changes probably related to strain, ground shaking, and to the presence of water in ponds are responsible for the loss of phase coherence near the fault (Figs. 2A and 3A). To map the surface rupture associated with the earthquake, we used the two-component offset field obtained by subpixel registrations of the radar amplitude images acquired before and after the earthquake (*14*). Unlike the interferometric phase, which is prone to coherence loss because of changes in surface conditions, the offset field provides surface displacement estimates in azimuth

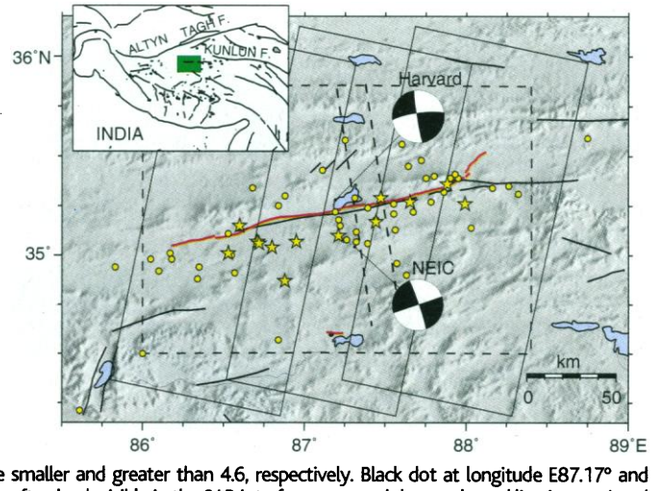

Fig. 1. Active fault map of the Manyi earthquake area over shaded 30 arc sec topographic map (GTOPO30). Faults in black are from (*8*). Red line is surface rupture mapped with offset fields (*14*). Focal mechanisms and epicenter locations determined by Harvard and by the National Earthquake Information Center (NEIC) are depicted (*7*). Yellow symbols show seismicity between 8 November 1997 and 31 December 1998 from NEIC catalog. Circles and stars depict aftershocks with magnitude smaller and greater than 4.6, respectively. Black dot at longitude E87.17° and latitude N34.60° is a shallow aftershock visible in the SAR interferogram, and the nearby red line is associated surface rupture (*27*). Boxes (solid line) represent the area covered by ERS tracks used here: track 76 (left), track 305 (center), and track 33 (right). Dashed box shows area covered by Fig. 2A. Dashed lines indicate location of profiles shown in Fig. 2B.

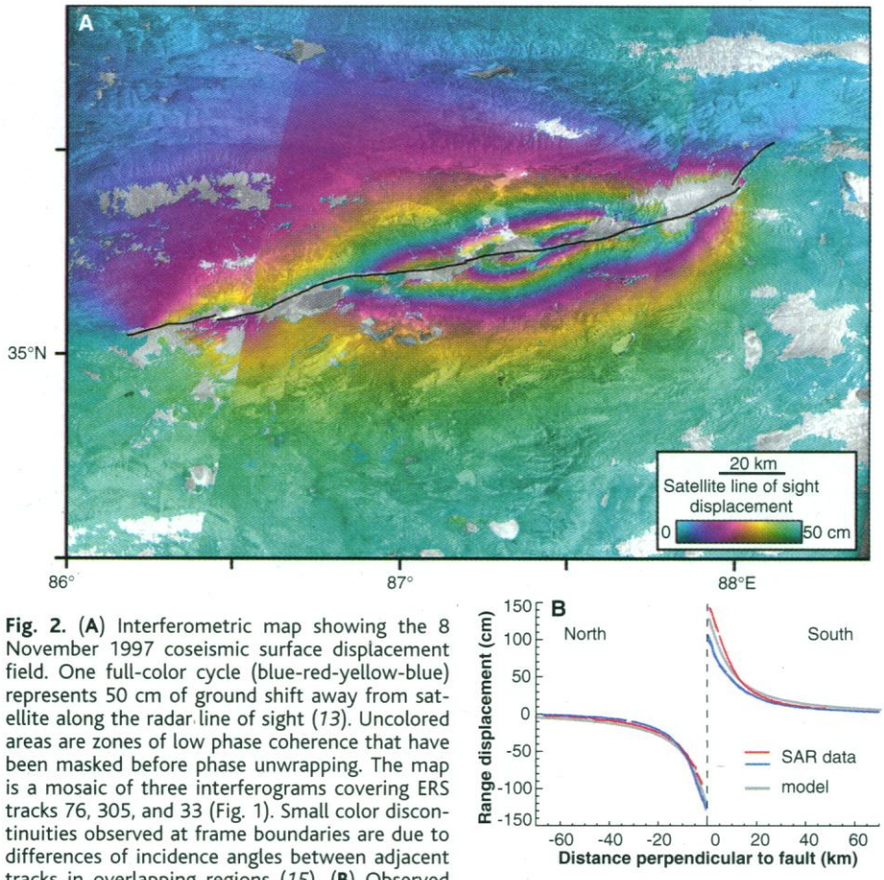

Fig. 2. (**A**) Interferometric map showing the 8 November 1997 coseismic surface displacement field. One full-color cycle (blue-red-yellow-blue) represents 50 cm of ground shift away from satellite along the radar line of sight (*13*). Uncolored areas are zones of low phase coherence that have been masked before phase unwrapping. The map is a mosaic of three interferograms covering ERS tracks 76, 305, and 33 (Fig. 1). Small color discontinuities observed at frame boundaries are due to differences of incidence angles between adjacent tracks in overlapping regions (*15*). (**B**) Observed (red and blue) and modeled (gray) line of sight displacement profiles perpendicular to fault. Red profile (left profile on Fig. 1) intersects the fault where maximum displacement is observed south of the fault. Blue profile (right profile on Fig. 1) is where maximum displacement is observed north of the fault. Fault is modeled in an elastic half-space (*1*) as a vertical plane, 8 km deep, with 7 m of slip uniformly distributed with depth.

[1]Jet Propulsion Laboratory, California Institute of Technology, Pasadena, CA 91109, USA. [2]Institut de Physique du Globe de Paris, France.

*To whom correspondence should be addressed at Jet Propulsion Laboratory MS 300-233, California Institute of Technology, 4800 Oak Grove Drive, Pasadena, CA 91109, USA. E-mail: gilles@altyn.jpl.nasa.gov

and range in the zone bordering the surface break. The dislocation produced by the earthquake was visible in the offset fields so that the 170-km-long surface break could be mapped with a precision of a few image pixels (Fig. 3B).

To produce the along-strike slip distribution curve, we first constructed two profiles of displacement with respect to the fixed, far-field reference south and north of the fault. For each point along the rupture, displacements observed in the nearest, coherent areas south and north of the fault were extrapolated to the fault (Fig. 3A). The line-of-sight projection of the slip distribution curve is the difference of the north and south displacement curves (Fig. 4A). In the regions of overlap between adjacent tracks, the observed range displacement is systematically larger in the eastern track than in the western track (Fig. 4A). This discrepancy is due to the difference in the line-of-sight incidence angle between adjacent orbits from where the ground is imaged (*15*). If we assume that the displacement of the ground is horizontal, it is possible to correct for the effect of line-of-sight projection by dividing the observed range change at each point by the sine of the local incidence angle (*16*). The result is the projection of the ground displacement on the horizontal axis perpendicular to the satellite track (cross-track) (Fig. 4B). The agreement between the cross-track displacement curves observed from adjacent orbits confirms that the displacement vector is horizontal along the fault trace (Fig. 4B).

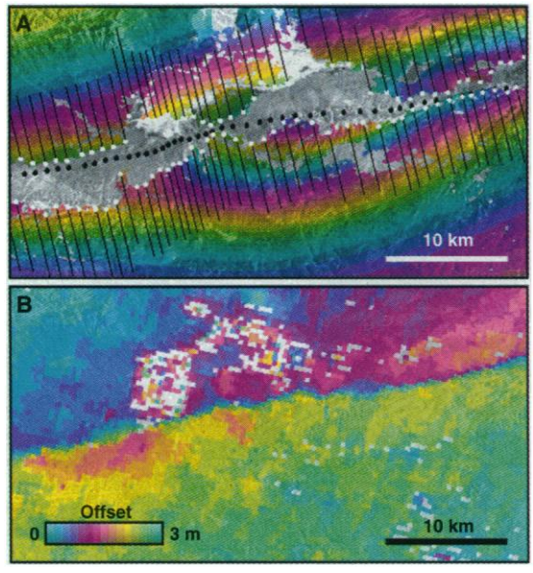

Fig. 3. (**A**) Detail of interferogram shown in Fig. 2A centered on surface rupture at longitude 87.3°. Black dots indicate surface rupture as mapped with offset fields (*14*). Range displacement is measured north and south of the fault at white dots, and values are extrapolated up to the rupture with the displacement gradient estimated along line segments (black lines). (**B**) Detail of the offset field in azimuth (*14*) covering the same area as in (A). The surface break follows the discontinuity in the offset field. White pixels over the dry lake area north of the fault are erroneous offset estimates attributable to lack of features in amplitude image.

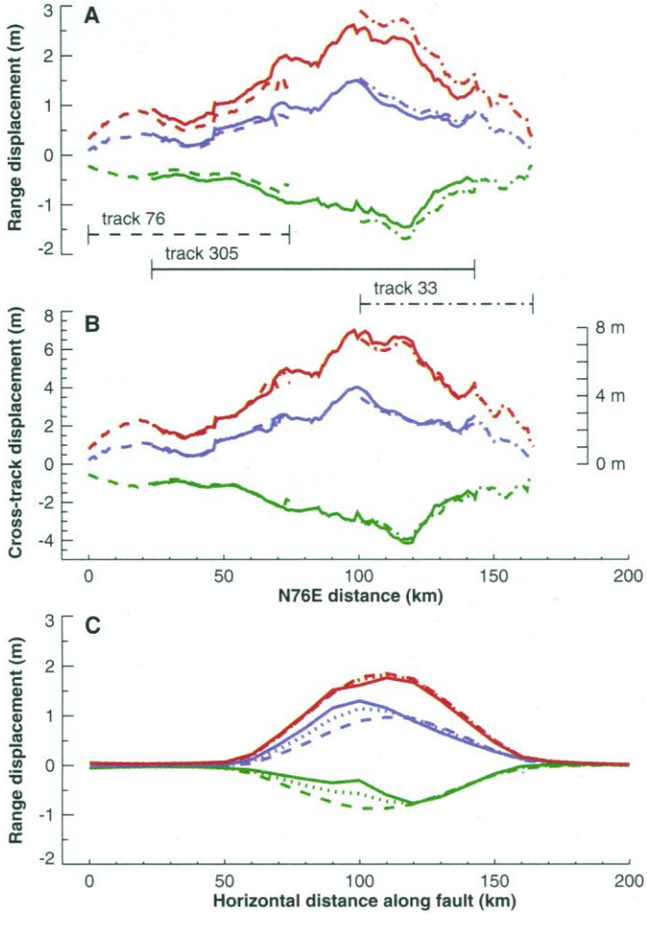

Fig. 4. (**A**) Observed range displacement distribution profiles along south (blue) and north (green) sides of fault. Fault-slip distribution (relative displacement between north and south sides) is shown in red. (**B**) Same as (A) for cross-track component of surface displacement. Profiles are obtained by normalizing the profiles shown in (A) by the sine of the incidence angle (*13*). For horizontal surface displacement, the normalized quantity is independent of the incidence angle. The 0 to 8 m vertical scale indicates corresponding strike-slip displacement on the fault. (**C**) Modeled, along-strike range displacement profiles assuming linear and nonlinear elastic crust. Colors are as in (A). Dashed lines correspond to the linear (Ec/Ed = 1) case. Dotted lines (Ec/Ed = 2) and solid lines (Ec/Ed = 4) correspond to nonlinear cases (see text). A constant incidence angle of 23° (*13*) is assumed for three-component displacement vector projection. Profiles are measured at a distance of 5 km from the fault.

The observed slip distribution is bimodal. The main event ruptured the eastern 150-km-long section of the fault with a maximum strike-slip offset of 7 m. A subevent ruptured the western 40-km-long section of the fault with a maximum strike-slip offset of 2.6 m. If we assume a uniform slip distribution over a depth of 8 km and an elastic shear modulus of 3.3×10^{10} N/m^2, the main event implies a geodetic moment of 1.4×10^{20} Nm, consistent with the seismic data (*17*).

The north and south along-strike displacement profiles show a marked asymmetry with respect to the fault. The profiles have a triangular shape between 50 and 150 km, but the maximum displacement of the southern side occurs 100 km from the western end of the fault, 20 km west of where it occurs along the northern side (Fig. 4, A and B). The north and south displacement curves are the symmetric images of one another with respect to the point located at 110 km, 0 cm on the plots of Fig. 4, A and B. Such a pattern cannot be accounted for by models based on linear elastic theory (*18*).

A possible explanation for this asymmetry is the presence of cracks in the crust. The effect of cracks in an elastic medium is to reduce its rigidity (*19*). This effect is nonlinear and depends on the sign of the effective normal stress resolved on the crack plane. Cracks would open in a tensile stress regime to a greater extent than they would close under a compressive regime of the same magnitude. Furthermore, new cracks can be created in tension but not in compression. Thus, the rigidity of the crust in compression should

be larger than its rigidity in tension. Such a nonlinear elastic property has been observed on many crustal rock samples in laboratory tests and in borehole measurements (*3*).

To test the effect of nonlinearity on the static displacement field produced by a strike-slip dislocation in an elastic medium, we used a three-dimensional finite element code (*20*) and assumed different values of the Young's modulus in compression and tension as a first approximation of the dependence of the Young's modulus on the minor principal stress. We modeled the earthquake dislocation as a 100-km-long and 15-km-wide vertical fault plane. The imposed strike-slip distribution has a trapezoidal shape with a constant maximum value of 7 m along the 20-km-long central section, linearly decreasing to 0 m toward the two ends of the fault. As a double couple mechanism, the planar fault geometry and the symmetry of slip distribution define four quadrants in the elastic half-space, separated by the fault plane and the auxiliary plane. For an east-west, left-lateral, strike-slip fault, the northeast and southwest quadrants are dilational and the northwest and southeast quadrants are compressional. We assigned different values of the Young's modulus to the compressional and dilational quadrants and compared three cases (*21*). The first case is the linear case where compressional (Ec) and dilational (Ed) Young's moduli are equal, as in the analytic solution (*1*). The two other cases are nonlinear and assume compressional Young's modulus values twice and four times larger than the tensional Young's modulus value. The linear case shows a slight asymmetry between the two curves with the maximum range displacement in the south occurring ~10 km east of where it is occurring on the north side (Fig. 4C). This small asymmetry is in the opposite direction to the observed asymmetry and is due to the effect of projection of the three-component displacement vector on the radar line of sight (*22*). The nonlinear cases (Ec/Ed = 2 and 4) lead to a larger asymmetry of the fault-parallel profiles, similar to the asymmetry of the observed profiles (Fig. 4, A and C). North and south of the fault, the location of the maximum displacement is shifted toward the tensile, weaker quadrant.

The north-south asymmetry of the displacement field can also be seen in the interferometric map (Fig. 2, A and B). The core of the contour lines (fringes) in the south appears to be centered 20 km west of where it is centered on the north side of the fault. This asymmetry tends to disappear as the distance to the fault increases, suggesting that nonlinear elasticity is most effective in the shallow crust (~3 to 5 km).

Crustal fluids at lithostatic pressure are required to maintain Mode-1 deformation of cracks effective at depth. Hydrological studies have shown that earthquake strain can mobilize crustal fluids to depths of 5 km or more (*23*). However, processes involving crustal fluid flow have relaxation times on the order of a few days to a year, depending on cracks connectivity and the porosity and permeability of the rocks (*23*, *24*). The SAR data acquired on ERS tracks 76, 305, and 33 used in this study cover 8, 24, and 40 days of the postseismic period, respectively (*10*). The agreement between sections of the displacement curves observed from adjacent orbits in overlapping parts of the satellite swaths (Fig. 4B) indicates that the observed displacement was not affected by any relaxation process during those periods of observation. Thus, the observed asymmetry of the displacement field near the fault has to be explained by a short-term process associated with the dislocation. These findings suggest that, at shallow depth (<3 km), efficient interconnection between cracks and the fact that some cracks may not be completely filled with fluids lead to a short-term, nonlinear elastic response of the crust to coseismic stress changes (*25*). However, the short-term response does not preclude longer-term relaxation of crustal fluid pressure gradients contained within less-connected cracks, especially at greater depth (>3 km). The geodetic signature of such processes is not observed in the along-strike displacement profiles because of the short period of observation after the earthquake and the fact that processes occurring at greater depth have a small influence on the surface displacement field at short distance from the fault.

We conclude that nonlinear elasticity related to the presence of cracks in the shallow crust provides a plausible explanation for the observed asymmetric displacement pattern across the Manyi earthquake fault. Modeling suggests that a ratio of 2 to 4 between compressional and extensional Young's moduli in the shallow part of the seismogenic crust can account for the radar observations. Although extrapolating values of elastic parameters derived from laboratory measurements to large volumes of crust must be done with caution, a contrast of 2 to 4 between compressional and tensional rigidity constants is commonly observed in laboratory test samples (*3*).

References and Notes

1. Y. Okada, *Bull. Seismol. Soc. Am.* **75**, 1135 (1985).
2. See, for example, K. W. Hudnut *et al.*, *ibid.* **84**, 625 (1994); J. Freymuller, N. E. King, P. Segall, *ibid.*, p. 646.
3. Many crustal rocks exhibit nonlinear elastic properties with a Young's modulus dependent on the confining pressure. Tests on laboratory samples showed that rocks such as sandstone, marble, limestone, quartzite, and granite have a Young's modulus in tension smaller than the Young's modulus in compression in a ratio ranging from 1/2 to 1/10 [J. C. Jaeger and N. G. Cook, *Fundamentals of Rocks Mechanics* (Chapman & Hall, London, ed. 3, 1979), chaps. 10 and 12; B. C. Haimson and T. M. Tharp, *Soc. Petrol. Eng. J.* **14**, 145 (1974); F. K. Khan and F. K. Irani, *Mech. Mater.* **6**, 271 (1988); B. Stimpson and R. Chen, *Can. Geotech. J.* **30**, 338 (1993); E. T. Brown, J. W. Bray, F. J. Santarelli, *Rock Mech. Rock Eng.* **3**, 189 (1989)].
4. Current geodetic techniques are based on arrays of a few tens of benchmarks with station spacing ranging from tens of meters for small-aperture trilateration arrays [G. A. Sylvester, *Geophys. Res. Lett.* **20**, 1079 (1993)] to ~10 km or more for global positioning system networks [for example, Z. K. Shen *et al.*, *Bull. Seismol. Soc. Am.* **84**, 780 (1994); F. K. Wyatt, D. C. Agnew, M. Gladwin, *ibid.*, p. 768].
5. The advantage of SAR interferometry over ground-based geodetic techniques is in providing spatially continuous maps of surface displacement over broad areas [(*26*); H. Gabriel, R. Goldstein, H. Zebker, *J. Geophys. Res.* **94**, 9183 (1989); H. Zebker *et al.*, *ibid.* **99**, 19617 (1994)]. The interferometric maps we generated here cover three swaths of 100 km in width and have a pixel size of ~90 m on the ground, after data averaging and geocoding.
6. Landsat images reveal quaternary faulting in the area of Tibet extending west of the western end of the Kunlun fault and south of the Altyn Tagh fault including east-northeast strike-slip faults and north-south normal faults [(*8*); R. Armijo *et al.*, *J. Geophys. Res.* **94**, 2787 (1989)].
7. The Harvard centroid moment tensor solution: strike = 262°, dip = 79°, rake = 4°, depth = 15 km, and moment = 2.8×10^{20} nm; the National Earthquake Information Center (NEIC) focal mechanism: strike = 71°, dip = 90°, rake = 4°, depth = 29 km, and moment = 1.5×10^{20} Nm. Both mechanisms indicate mostly left-lateral, strike-slip motion on an east-northeast striking fault.
8. P. Tapponnier and P. Molnar, *J. Geophys. Res.* **82**, 2905 (1977).
9. The seismicity catalog of the NEIC includes 80 aftershocks in 1997 and 1998, 16 of which have Mw > 4.5. The largest event listed (Mw = 5.3) occurred on 9 November 1997, ~150 km south of the surface rupture. We identified in the radar data the surface displacement of a shallow earthquake that could not be associated with any of the aftershock locations listed in the NEIC catalog (*27*) (Fig. 1).
10. ERS-2 SAR data were acquired on 16 March and 16 November 1997 for track 76, 19 August and 2 December 1997 for track 305, and 22 May and 18 December 1997 for track 33 (Fig. 1). Each pair of raw SAR images was processed to an interferogram with the JPL radar processing software ROI−PAC.
11. In each SAR image pixel, the phase value represents a measure modulo-2π of the distance between the radar antenna and the ground. An interferogram is obtained by averaging the product of one complex SAR image and the complex conjugate of another image, after subpixel coregistration. The phase of each pixel in an interferogram is the difference of the phase of the corresponding pixels in the two SAR images. The interferometric phase depicts variations of the antenna-ground path-length difference between the two images.
12. The topographic signal can be removed from an interferogram by simulating the topographic phase with a digital elevation model and the geometric parameters defining the configuration of the orbits at times of acquisitions of the data [(*26*); M. Murakami *et al.*, *J. Geophys. Res.* **101**, 8605 (1996)]. For this study, we used the 90-m-resolution Digital Terrain Elevation Data (DTED) (National Imagery and Mapping Agency).
13. For ERS, the satellite line of sight is nearly perpendicular to the orbit. On descending passes, the observation is made from the southeast with an incidence angle of 18.5° in near range (east edge of image) and 27° in far range (west edge of image) [European Space Agency, ERS-1 System (ESA Publication Division, ESTEC, Noordwijk, Netherlands, 1992)].
14. Interferometric processing of SAR images requires subpixel registration of the two images. This is achieved by searching for local peaks of amplitude correlation between the two images. This procedure provides us with azimuth (parallel to satellite track) and range (perpendicular to satellite track) offset fields that reflect the geometric shift and distortions between the two images. Typical noise in offset fields in the present data is about 1/20th of the pixel size.

The size of an ERS SAR single-look pixel on the ground is 4 m in azimuth and 20 m in range. This technique is similar to the approach developed by R. E. Crippen [*Episodes* **15**, 56 (1992)] with visible satellite images (SPOT).
15. At 35°N latitude on descending orbit passes, the incidence angle difference between lines of sight of adjacent orbits varies from 4.6° to 4.9° between the far range (western edge) and the near range (eastern edge) of the area of swath overlap (*13*).
16. The line-of-sight projection of a displacement vector (e, n, u) in the local east, north, up reference frame is $r = [e\cos(\alpha) - n\sin(\alpha)]\sin(i) + u\cos(i)$, where α is the angle between the azimuthal direction of the displacement vector and the direction perpendicular to the satellite track, and i is the incidence angle (*13*). For horizontal displacement fields ($u = 0$), the observed cross-track component of the displacement vector is $r/\sin(i)$ and is independent of the incidence angle.
17. The source time function of the earthquake depicts a similar bimodal shape with a main pulse moment of $\sim 1.5 \times 10^{20}$ Nm in the first 30 s followed by a smaller pulse of 10 s [University of Michigan Web site: www.geo.lsa.umich.edu/SeismoObs/STF.html (1997); A. Velasco, personal communication (1998)].
18. Seismic and radar data indicate that only one fault was involved in the earthquake. Shear stress across the fault must be continuous (equilibrium conditions). Observed displacement asymmetry indicates that strain is not continuous across the fault. Thus, elastic properties must be different between the two sides of the fault. The particular form of asymmetry observed in the displacement curves (Fig. 4B) suggests that elastic properties are correlated with volume strain and not related to crustal heterogeneities along the rupture.
19. W. R. Delameter, G. Herrmann, D. M. Barnett, *J. Appl. Mech.* **47**, 74 (1975); E. R. Ivins and G. A. Lyzenga, *Philos. Trans. R. Soc. London Ser. A* **318**, 285 (1986).
20. F. Saucier, thesis, University of Oregon (1991).
21. This approach is akin to a first-order perturbation approach with respect to a linear model because we implicitly assume that the locations of compressional and tensile volumes are unchanged by nonlinearity.
22. Given the symmetry of the fault geometry and slip distribution of the model, the along-strike distribution of the fault-parallel, horizontal component of the displacement vector is symmetric with respect to the auxiliary plane and the distribution of the vertical component is antisymmetric. The line-of-sight projection of the vector combines all components of the displacement vector (*16*) and thus depicts the antisymmetry of its vertical component with respect to the auxiliary plane.
23. R. Muir-Wood and G. C. P. King, *J. Geophys. Res.* **98**, 22035 (1993).
24. A. Nur and J. R. Booker, *Science* **175**, 885 (1972); D. L. Anderson and J. H. Whitecomb, *J. Geophys. Res.* **80**, 1497 (1975); K. W. Hudnut, L. Seeber, J. Pacheo, *Geophys. Res. Lett.* **16**, 199 (1989); C. H. Scholz, *Geology* **2**, 551 (1974); J. B. Rundle and W. Thatcher, *Bull. Seismol. Soc. Am.* **70**, 1869 (1980); G. Peltzer, P. Rosen, F. Rogez, K. Hudnut, *Science* **273**, 1202 (1996).
25. A drop of seismic velocities at depths shallower than 3 to 5 km is observed in many places [P. Reasenberg and W. L. Ellsworth, *J. Geophys. Res.* **87**, 10637 (1982); A. W. Walter and W. D. Mooney, *Bull. Seismol. Soc. Am.* **72**, 1567 (1982); L. D. Dietz and W. L. Ellsworth, *Geophys. Res. Lett.* **17**, 1417 (1990); C. Dorbath, D. Oppenheimer, F. Amelung, G. King, *J. Geophys. Res.* **101**, 27917 (1996)] and is generally attributed to the presence of open cracks not saturated with fluids in the shallow crust.
26. D. Massonnet *et al.*, *Nature* **364**, 138 (1993).
27. At longitude E87.17° and latitude N34.60° the interferogram shows a double lobe, ~10-km-long pattern, with a maximum range change corresponding to ~10 cm of surface uplift and bounded to the north by an east-west, ~8-km-long line of phase discontinuity. We interpret this feature as the surface displacement field associated with a shallow earthquake having occurred between 19 August and 2 December 1997. The observed displacement and phase discontinuity suggest that the event has left-lateral and thrust components and a fault plane steeply dipping to the south (F. Crampé and G. Peltzer, in preparation). We note, however, that the geographic location of this feature is 30 km away from the nearest aftershock epicenter determined by the NEIC during the same period. This may be due either to large errors in the localization of aftershocks or to the fact that this shallow event occurred during the propagation of the main rupture, making its seismic record indistinguishable from that of the main event.

28. We thank P. Bernard, F. Cornet, E. Ivins, and H. Kanamori for fruitful discussions; P. Lundgren for help with the modeling; and two anonymous reviewers for constructive comments. ERS data were provided by the European Space Agency. Work for this study was done at the Jet Propulsion Laboratory, California Institute of Technology, under contract with NASA.

7 June 1999; accepted 11 August 1999

Measurements of Past Ice Sheet Elevations in Interior West Antarctica

Robert P. Ackert Jr.,[1]* David J. Barclay,[3] Harold W. Borns Jr.,[4] Parker E. Calkin,[6] Mark D. Kurz,[2] James L. Fastook,[5] Eric J. Steig[7]

A lateral moraine band on Mount Waesche, a volcanic nunatak in Marie Byrd Land, provides estimates of past ice sheet surface elevations in West Antarctica. Helium-3 and chlorine-36 surface exposure ages indicate that the proximal part of the moraine, up to 45 meters above the present ice surface, was deposited about 10,000 years ago, substantially later than the maximum ice extent in the Ross Embayment. The upper distal part of the moraine may record multiple earlier ice sheet high stands. A nonequilibrium ice sheet model predicts a delay of several thousand years in maximum ice levels at Mount Waesche relative to the maximum ice extent in the Ross Sea. The glacial geologic evidence, coupled with the ice sheet model, indicates that the contribution of the Ross Sea sector of the West Antarctic Ice Sheet to Holocene sea level rise was only about 3 meters. These results eliminate West Antarctic ice as the principle source of the large meltwater pulse during the early Holocene.

Knowledge of the past configurations and behavior of the West Antarctic Ice Sheet (WAIS) is necessary to calibrate glaciological models that attempt to predict future responses of the ice sheet and to quantify the contribution of the Antarctic ice sheets to eustatic sea level rise during the last deglaciation. Outlet glaciers in the Transantarctic Mountains were once dammed by thick grounded ice in the Ross Embayment, where only a floating ice shelf occurs today (*1*). In the McMurdo Sound region, ^{14}C and surface exposure ages on drift deposited by ice grounded in the Ross Sea date to the last glacial maximum (LGM) (*2*). Geophysical mapping of the Ross Sea floor (*3*) and ^{14}C ages on sediments overlying tills (*4*) demonstrate that grounded ice extended to near the continental shelf break at the LGM, over 1000 km beyond the present grounding line.

In contrast to its extent, direct evidence for the interior elevation of the WAIS has been quite uncertain. An ice sheet model constrained by the evidence from the Ross Embayment, trimlines in the Ellsworth Mountains, and striations on the Hobbs coast suggests that ice sheet domes in West Antarctica were 450 to 600 m higher during the LGM (*5*). However, the age of the trimlines and striations is uncertain, and this reconstruction may overestimate interior elevations (*5*). Total gas content from the Byrd ice core, which is largely a function of past atmospheric pressure (elevation of the site) (*6*), has been interpreted as indicating that ice elevations were ~200 m lower (*7*) and 400 to 500 m higher (*8*) during the LGM and early Holocene. Byrd core $\delta^{18}O$ data imply that ice elevations were ~500 m higher during the LGM (*9*). Here, we present new surface exposure ages from a lateral moraine band at Mount Waesche that directly date the most recent ice high stand in interior West Antarctica.

Mount Waesche is the southernmost volcano in the Executive Committee Range, a line of volcanoes that projects through the WAIS in Marie Byrd Land (Fig. 1). Regional ice flow is southward from a dome centered on the northern Executive Committee Range, where ice

[1]Massachusetts Institute of Technology/Woods Hole Oceanographic Institution Joint Program, MS 25, Clark 419, [2]Department of Marine Chemistry and Geochemistry, Woods Hole Oceanographic Institution, Woods Hole, MA 02543, USA. [3]Department of Geology, State University of New York at Cortland, Cortland, NY 13045, USA. [4]Institute for Quaternary Studies, [5]Department of Computer Science, University of Maine, Orono, ME 04469, USA. [6]Institute of Arctic and Alpine Research, University of Colorado, Boulder, CO 80309, USA. [7]Department of Earth and Environmental Science, University of Pennsylvania, Philadelphia, PA 19104–6316, USA.

*To whom correspondence should be addressed. E-mail: rackert@whoi.edu

References and Notes

[24] **Aftershocks Caused by Pore Fluid Flow?**
Amos Nur; John R. Booker
Science, New Series, Vol. 175, No. 4024. (Feb. 25, 1972), pp. 885-887.
Stable URL:
http://links.jstor.org/sici?sici=0036-8075%2819720225%293%3A175%3A4024%3C885%3AACBPFF%3E2.0.CO%3B2-F

[24] **Postseismic Rebound in Fault Step-Overs Caused by Pore Fluid Flow**
Gilles Peltzer; Paul Rosen; Francois Rogez; Ken Hudnut
Science, New Series, Vol. 273, No. 5279. (Aug. 30, 1996), pp. 1202-1204.
Stable URL:
http://links.jstor.org/sici?sici=0036-8075%2819960830%293%3A273%3A5279%3C1202%3APRIFSC%3E2.0.CO%3B2-I